GEOPHYSICS, VOL. 82, NO. 3 (MAY-JUNE 2017); P. D171–D186, 12 FIGS., 1 TABLE.
10.1190/GEO2016-0480.1

Hydraulic fracture diagnostics from Krauklis-wave resonance and tube-wave reflections

Chao Liang[1], Ossian O'Reilly[2], Eric M. Dunham[3], and Dan Moos[4]

ABSTRACT

Fluid-filled fractures support guided waves known as Krauklis waves. The resonance of Krauklis waves within fractures occurs at specific frequencies; these frequencies, and the associated attenuation of the resonant modes, can be used to constrain the fracture geometry. We use numerical simulations of wave propagation along fluid-filled fractures to quantify fracture resonance. The simulations involve solution of an approximation to the compressible Navier-Stokes equation for the viscous fluid in the fracture coupled to the elastic-wave equation in the surrounding solid. Variable fracture aperture, narrow viscous boundary layers near the fracture walls, and additional attenuation from seismic radiation are accounted for in the simulations. We then determine how tube waves within a wellbore can be used to excite Krauklis waves within fractures that are hydraulically connected to the wellbore. The simulations provide the frequency-dependent hydraulic impedance of the fracture, which can then be used in a frequency-domain tube-wave code to model tube-wave reflection/transmission from fractures from a source in the wellbore or at the wellhead (e.g., water hammer from an abrupt shut-in). Tube waves at the resonance frequencies of the fracture can be selectively amplified by proper tuning of the length of a sealed section of the wellbore containing the fracture. The overall methodology presented here provides a framework for determining hydraulic fracture properties via interpretation of tube-wave data.

INTRODUCTION

Hydraulic fracturing is widely used to increase the permeability of oil and gas reservoirs. This transformative technology has enabled production of vast shale oil and gas resources. Although engineers now have optimal control of well trajectories, the geometry (length, height, and aperture) of hydraulic fractures is still poorly known, which poses a challenge for optimizing well completion. Monitoring hydraulic fracture growth is desirable for many reasons. Tracking the length of fractures ensures that multiple subparallel fractures remain active, rather than shielding each other through elastic interactions. It might also be used to prevent fractures in nearby wells from intersecting one another. In addition, the ability to measure fracture geometry would facilitate estimates of the stimulated volume and could be used to help guide the delivery of proppant.

Due to their sensitivity to properties of the surrounding formation and fractures intersecting the wellbore, tube waves or water hammer propagating along the well are widely used for formation evaluation and fracture diagnostics (Paillet, 1980; Paillet and White, 1982; Holzhausen and Gooch, 1985a, 1985b; Holzhausen and Egan, 1986; Hornby et al., 1989; Tang and Cheng, 1989; Paige et al., 1992, 1995; Kostek et al., 1998a, 1998b; Patzek and De, 2000; Henry et al., 2002; Ziatdinov et al., 2006; Ionov, 2007; Wang et al., 2008; Derov et al., 2009; Mondal, 2010; Bakku et al., 2013; Carey et al., 2015; Livescu et al., 2016). Here, we are specifically concerned with low-frequency tube waves having wavelengths much greater than the wellbore radius. In this limit, tube waves propagate with minimal dispersion at a velocity slightly less than the fluid sound speed (Biot, 1952). Besides excitation from sources within the well or at the wellhead, tube waves can be generated by incident seismic waves from the surrounding medium (Beydoun et al., 1985; Schoenberg, 1986; Ionov

Manuscript received by the Editor 9 September 2016; published online 21 March 2017.
[1]Stanford University, Department of Geophysics, Stanford, California, USA. E-mail: chao2@stanford.edu.
[2]Formerly Baker Hughes, Palo Alto, California, USA; presently Stanford University, Department of Geophysics, Stanford, California, USA. E-mail: ooreilly@stanford.edu.
[3]Stanford University, Department of Geophysics, Stanford, California, USA and Stanford University, Institute for Computational and Mathematical Engineering, Stanford, California, USA. E-mail: edunham@stanford.edu.
[4]Formerly Baker Hughes, Palo Alto, California, USA, presently . E-mail: dbmoos1@earthlink.net.

and Maximov, 1996; Bakku et al., 2013) and by sources within hydraulic fractures (Krauklis and Krauklis, 1998; Ionov, 2007; Derov et al., 2009). Furthermore, tube waves incident on a fracture in hydraulic connection to the wellbore will reflect and transmit from the fracture, with frequency-dependent reflection/transmission coefficients. As described in more detail below, these reflected and transmitted tube waves carry information about fracture geometry.

A closely related concept is that of hydraulic impedance testing (Holzhausen and Gooch, 1985a), initially developed to estimate the geometry of axial fractures (fractures in the plane of the wellbore). This method, using very low frequency tube waves or water-hammer signals, was validated through laboratory experiments (Paige et al., 1992) and applied to multiple field data sets (Holzhausen and Egan, 1986; Paige et al., 1995; Patzek and De, 2000; Mondal, 2010; Carey et al., 2015). The method is typically presented using the well-known correspondence between hydraulics and electrical circuits, with hydraulic impedance defined as the ratio of pressure to volumetric flow rate (velocity times the cross-sectional area). The fracture consists of a series connection of resistance (energy loss through viscous dissipation and seismic radiation), capacitance (energy stored in elastic deformation of the solid and compression/expansion of the fluid), and inertance (kinetic energy of the fluid), which can be combined into a complex-valued hydraulic impedance of the fracture. The hydraulic impedance is then related to the geometry of the fractures (Holzhausen and Gooch, 1985a; Paige et al., 1992; Carey et al., 2015). However, this method, at least as presented in the literature thus far, assumes a quasi-static fracture response when relating (spatially uniform) pressure in the fracture to the fracture volume. This assumption is valid only for extremely low frequencies, and it neglects valuable information at higher frequencies in which there exists the possibility of a resonant fracture response associated with waves propagating within the fracture. The treatment of dissipation from fluid viscosity is similarly overly simplistic.

Thus, a more rigorous treatment of the fracture response is required, motivating a more nuanced description of the dynamics of fluid flow within the fracture and of its coupling to the surrounding elastic medium over a broader range of frequencies. The key concept here is a particular type of guided wave that propagates along fluid-filled cracks. These waves, known as crack waves or Krauklis waves, have been studied extensively in the context of the oil and gas industry, volcano seismology, and other fields (Krauklis, 1962; Paillet and White, 1982; Chouet, 1986; Ferrazzini and Aki, 1987; Korneev, 2008, 2010; Yamamoto and Kawakatsu, 2008; Dunham and Ogden, 2012; Lipovsky and Dunham, 2015; Nikitin et al., 2016). At the frequencies of interest here (approximately 1–1000 Hz), they are anomalously dispersed waves of opening and closing that propagate along fractures at speeds approximately 10–1000 m/s. Experimental studies have confirmed the existence and propagation characteristics of these waves (Tang and Cheng, 1988; Nakagawa, 2013; Shih and Frehner, 2015; Nakagawa et al., 2016). Counterpropagating pairs of Krauklis waves form standing waves (eigenmodes) of fluid-filled cracks, and the resonance frequencies and decay rates of these modes are sensitive to the fracture length and aperture. Krauklis waves are thought to be responsible for the long period and very long period seismicity at active volcanoes (Aki et al., 1977; Chouet, 1988), and they have been suggested as a possible explanation for harmonic seismic signals recorded during hydraulic fracturing treatments (Ferrazzini and Aki, 1987; Tary et al., 2014). Most studies of Krauklis waves have been analytical or semianalytical, with a major focus on deriving dispersion relations for waves in infinitely long fluid layers of uniform width. A notable exception is the work of Frehner and Schmalholz (2010) and Frehner (2013), in which finite elements in two dimensions were used to study Krauklis waves in finite-length fractures with variable aperture. Using a numerical approach provides a means to investigate the reflection and scattering of Krauklis waves at fracture tips (Frehner and Schmalholz, 2010) and the excitation of Krauklis waves by incident seismic waves (Frehner, 2013). However, these studies did not consider the interaction between the Krauklis and tube waves, which is a central focus of our study.

Mathieu and Toksoz (1984) were the first to pose the mathematical problem of tube-wave reflection/transmission across a fracture in terms of the fracture impedance. In this work, we define the fracture hydraulic impedance in the frequency domain as

$$Z_f(\omega) = \frac{\hat{p}_f(\omega)}{\hat{q}_f(\omega)}, \tag{1}$$

where $\hat{p}_f(\omega)$ and $\hat{q}_f(\omega)$ are the Fourier transforms of the pressure and volumetric flow rate into the fracture, both evaluated at the fracture mouth. The Fourier transform of some function $g(t)$ is defined as

$$\hat{g}(\omega) = \int_{-\infty}^{\infty} g(t) e^{i\omega t} dt. \tag{2}$$

Mathieu and Toksoz (1984) treated the fracture as an infinite fluid layer or a permeable porous layer with the fluid flow being described by Darcy's law. The fracture hydraulic impedance built on Darcy's law was then replaced with analytic solutions based on the dispersion relation for acoustic waves in an inviscid (Hornby et al., 1989) or viscous (Tang and Cheng, 1989) fluid layer bounded by rigid fracture walls. Later studies established that elasticity of the fracture wall rock significantly changes the reflection and transmission across a fracture (Tang, 1990; Kostek et al., 1998a, 1998b). The arrival time and amplitude of reflected tube waves can be used to infer the location and effective aperture of fractures (Medlin and Schmitt, 1994). However, most of these models assume an infinite fracture length, as is well-justified (Hornby et al., 1989) for the high frequencies (approximately 1 kHz) that were the focus of these studies. By focusing instead on lower frequencies (< 100 Hz) and considering Krauklis waves reflected from the fracture tip, Henry et al. (2002) and Henry (2005) argued that reflection/transmission of tube waves is affected by the resonance of the fracture, and this consequently provides sensitivity to fracture length.

One approach to account for the finite extent of the fracture is to use the dispersion relation for harmonic Krauklis waves to determine the eigenmodes of a circular disk-shaped fracture of uniform aperture with a zero radial velocity boundary condition at the edge of the disk (Hornby et al., 1989; Henry et al., 2002; Henry, 2005; Ziatdinov et al., 2006; Derov et al., 2009). This treatment fails to account for the decreased aperture near the fracture edge, which decreases the Krauklis-wave phase velocity and increases the viscous dissipation. It furthermore implicitly assumes perfect reflection from the fracture edge, thereby neglecting attenuation from seismic-wave radiation. Recent studies have established the importance of this attenuation mechanism (Frehner and Schmalholz, 2010; Frehner, 2013).

In this work, we examine how Krauklis waves propagating in fluid-filled fractures, as well as tube-wave interactions with fractures, can be used to infer fracture geometry. Figure 1 shows the system. The overall problem is to determine the response of the coupled fracture-wellbore system to excitation at the wellhead, within the wellbore, or at the fracture mouth. Other excitation mechanisms, including sources in the fracture or incident seismic waves from some external source in the solid (e.g., microseismic events or active sources), are not considered here. The fracture and wellbore are coupled in several ways, the most important of which is through the direct fluid contact at the fracture mouth. Pressure changes at this junction, for instance, due to tube waves propagating along the wellbore, will excite Krauklis waves in the fracture. Similarly, fluid can be exchanged between the wellbore and fracture. Other interactions, such as through elastic deformation of the solid surrounding the wellbore and fracture, are neglected in our modeling approach.

By making this approximation, and by further assuming that all perturbations are sufficiently small so as to justify linearization, the response of the coupled fracture-wellbore system can be obtained in two steps (Mathieu and Toksoz, 1984; Hornby et al., 1989; Kostek et al., 1998a; Henry, 2005). In the first step, we determine the response of the fracture, in isolation from the wellbore, to excitation at the fracture mouth. Specifically, we calculate the (frequency-dependent) hydraulic impedance of the fracture, as defined in equation 1, using high-resolution finite-difference simulations of the dynamic response of a fluid-filled fracture embedded in a deformable elastic medium. This provides a rigorous treatment of viscous dissipation and seismic radiation along finite-length fractures with possibly complex geometries, including variable aperture. The numerical solutions are compared with semianalytic solutions based on dispersion relations for harmonic waves propagating along an infinitely long fluid layer of uniform width. In the second step, we solve the tube-wave problem in the frequency domain, in which the fracture response is captured through the fracture hydraulic impedance, and then it is converted to the time domain by inverting the Fourier transforms. The fracture response, as embodied by the fracture hydraulic impedance, features multiple resonance peaks associated with the eigenmodes of the fracture. The frequencies and attenuation properties of these modes are sensitive to the fracture length and aperture. These resonances furthermore make the tube-wave reflection/transmission coefficients dependent on frequency, with the maximum reflection at the resonance frequencies of the fracture. We close by presenting synthetic pressure seismograms for tube waves within the wellbore, along with a demonstration of the sensitivity of these signals to fracture geometry.

FLUID-FILLED FRACTURES

Fluid governing equations and numerical simulations of fluid-filled fractures

The first step in the solution procedure outlined above is to determine the hydraulic impedance of the fracture. In fact, we find it more convenient to work with a nondimensional quantity proportional to the reciprocal of the fracture hydraulic impedance, which we refer to as the fracture transfer function $F(\omega)$. Although the fracture hydraulic impedance diverges in the low-frequency limit, the fracture transfer function goes to zero in a manner that captures the quasi-static fracture response used in the original work on hydraulic impedance testing.

The fluid-filled fracture system is described by the elastic-wave equation, governing displacements of the solid, and the compressible Navier-Stokes equation for the viscous fluid in the fracture. In this work, we use a linearized, approximate version of the Navier-Stokes equation that retains only the minimum set of terms required to properly capture the low-frequency response of the fluid (Lipovsky and Dunham, 2015). By low frequency, we mean $\omega w_0/c_0 \ll 1$, where ω is the angular frequency, w_0 is the crack aperture or width (the two terms are used interchangeably hereafter), and c_0 is the fluid sound speed. For $w_0 \sim 1$ mm and $c_0 \sim 10^3$ m/s, frequencies must be smaller than approximately 1 MHz. This is hardly a restriction because fracture resonance frequencies are typically well less than approximately 100 Hz. The derivation of the governing equations and details of the numerical treatment (using a provably stable, high-order-accurate finite-difference discretization) are discussed by Lipovsky and Dunham (2015) and O. O'Reilly et al. (personal communication, 2017). Here, we explain the geometry of our simulations and then briefly review the fluid governing equations within the fracture to facilitate the later discussion of Krauklis waves and the fracture transfer function.

Although a solution to the 3D problem is required to quantify how the fracture transfer function depends on the fracture length, height, and width, in this preliminary study, we instead use a 2D plane strain model (effectively assuming an infinite fracture height). We anticipate that this 2D model will provide a reasonable description of axisymmetric fractures, such as the one illustrated in Figure 1, although some differences should be expected from the differing nature of plane waves and axisymmetric waves. However, the procedure for using the fracture transfer function, obtained from numerical simulations, to solve the coupled wellbore-fracture problem, is completely general, as are the overall qualitative results concerning matched resonance that are discussed in the context of tube-wave interactions with fractures. Finally, when the fracture transfer functions from 3D simulations are available, the coupling solution procedure can be used with no additional modifications.

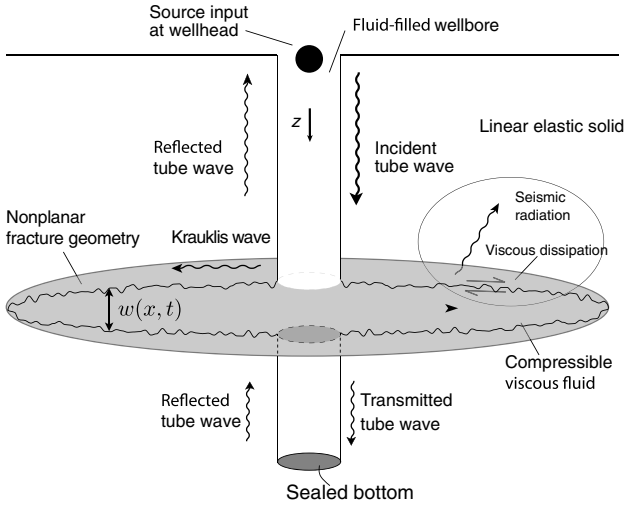

Figure 1. Tube waves, excited at the wellhead, are incident on a fluid-filled fracture intersecting the wellbore. Pressure changes and fluid-mass exchange between the wellbore and fracture excite Krauklis waves within the fracture, leading to partial reflection of the tube waves and dissipation of energy.

Returning to the 2D plane strain problem, let x be the distance along the fracture and y be the distance perpendicular to the fracture; the origin is placed at the fracture mouth, where we will later couple the fracture to a wellbore. We use an approximation similar in many respects to the widely used lubrication approximation for thin viscous layers (Batchelor, 2000), although we retain terms describing fluid inertia and compressibility. In the low-frequency limit ($\omega w_0/c_0 \ll 1$), the y-momentum balance establishes the uniformity of pressure across the width of the fracture (Ferrazzini and Aki, 1987; Korneev, 2008; Lipovsky and Dunham, 2015). The linearized x-momentum balance is

$$\rho\frac{\partial v}{\partial t}+\frac{\partial p}{\partial x}=\mu\frac{\partial^2 v}{\partial y^2}, \tag{3}$$

where $v(x,y,t)$ is the particle velocity in the x-direction, $p(x,t)$ is the pressure, and ρ and μ are the fluid density and dynamic viscosity, respectively. We have retained only the viscous term corresponding to shear along planes parallel to $y=0$; scaling arguments show that other viscous terms are negligible in comparison for this class of problems (Lipovsky and Dunham, 2015). The initial and perturbed fracture widths are defined as

$$w_0(x)=w_0^+(x)-w_0^+(x), \tag{4}$$

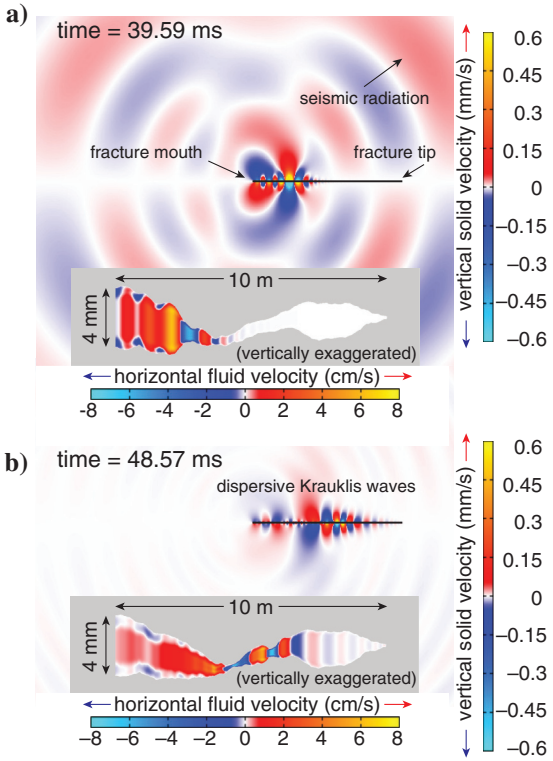

Figure 2. Snapshots from simulation of Krauklis and elastic waves excited by an imposed pressure chirp at the fracture mouth, for a 10 m long fracture with a 4 mm width at the fracture mouth. The background shows the solid response (to scale), and the inset shows the fluid response (vertically exaggerated). Colors in the solid show the particle velocity in the direction normal to the fracture walls; discontinuities across the fracture indicate opening/closing motions characteristic of Krauklis waves. Colors in the fluid show the particle velocity; note the narrow viscous boundary layers near the nonplanar fracture walls. The multimedia version of Figure 2 can be accessed through this link: s1.mp4.

$$w(x,t)=w^+(x,t)-w^-(x,t). \tag{5}$$

Note that w_0 refers to the full width, whereas some previous work (Lipovsky and Dunham, 2015) used this to refer to the half-width. Combining the linearized fluid mass balance with a linearized equation of state, we obtain

$$\frac{1}{K}\frac{\partial p}{\partial t}+\frac{1}{w_0}\frac{\partial w}{\partial t}=-\frac{1}{w_0}\frac{\partial (uw_0)}{\partial x}, \tag{6}$$

where

$$u(x,t)=\frac{1}{w_0(x)}\int_{w_0^-(x)}^{w_0^+(x)} v(x,y,t)dy \tag{7}$$

is the x-velocity averaged over the fracture width and K is the fluid bulk modulus. The fluid sound speed is $c_0=\sqrt{K/\rho}$. Accumulation/loss of fluid mass at some location in the fracture can be accommodated by either compressing/expanding the fluid (the first term on the left side of equation 6) or opening/closing the fracture walls (the second term on the left side of equation 6). The latter is the dominant process at the low frequencies of interest in this study.

Coupling between the fluid and solid requires balancing tractions and enforcing continuity of normal and tangential particle velocity on the fracture walls (i.e., the kinematic and no-slip conditions). At the fracture mouth, pressure is prescribed; zero velocity is prescribed at the fracture tip. At the outer boundaries of the solid domain, absorbing boundary conditions are used to suppress artificial reflections. The computational domain in both directions is 12 times the length of the fracture so as to fully capture the quasi-static displacements in the solid and to further minimize boundary reflections.

Spatial variations in the fracture width are captured through $w_0(x)$. A uniformly pressurized fracture in an infinite medium has an elliptical opening profile, $w_0(x)\propto\sqrt{L^2-x^2}$, and a stress singularity at the fracture tips. Here, we use a related solution for $w_0(x)$ in which closure at the tip occurs in a more gradual manner so as to remove that singularity. In particular, we use expressions for $w_0(x)$ from a cohesive zone model (Chen and Knopoff, 1986), appropriately modified from antiplane shear to plane strain by replacement of the shear modulus G with $G^*=G/(1-\nu)$, where ν is Poisson's ratio. The cohesive zone region is approximately 25% of the fracture length. In addition, we blunt the fracture tip so that it has a finite width (usually a small fraction of the maximum width at the fracture mouth, unless otherwise indicated).

Figure 2 shows snapshots of the numerical simulation of Krauklis waves propagating along a fluid-filled fracture. For this example only, we add to $w_0(x)$ a band-limited self-similar fractal roughness, as in Dunham et al. (2011) with an amplitude-to-wavelength ratio of 10^{-2}, similar to what is observed for natural fracture surfaces and faults (Power and Tullis, 1991; Candela et al., 2012). Material properties used in this and other simulations are given in Table 1. The fracture opens in regions of converging fluid flow, and it contracts where the flow diverges. Krauklis waves with different wavelengths separate as they propagate along the fracture due to dispersion. Krauklis waves arise from the combined effects of fluid inertia and the restoring force from fracture wall elasticity. Because the elastic wall is more compliant at longer wavelengths, all else being equal, long-wavelength waves experience smaller restoring forces and hence propagate more slowly. Elastic waves in the solid are excited

at the fracture mouth and along the fracture due to inertia of the solid during Krauklis-wave reflection from the fracture tip and fracture mouth. Note that elastic waves propagate nearly an order of magnitude faster than Krauklis waves; this is evident in Figure 2a. As seen in the Figure 2 insets, viscous effects are primarily restricted to narrow boundary layers near the fracture walls and there can even be flow reversals and nonmonotonic velocity profiles. The decreased width near the fracture tip decelerates the Krauklis waves and enhances the viscous dissipation in the near-tip region. After being reflected multiple times, pairs of counterpropagating Krauklis waves form standing waves along the fracture, which set the fluid-filled fracture into resonance. Shorter period modes are damped out first, by the viscous dissipation and seismic radiation, leaving long-period modes with wavelengths of the order of the fracture length. The frequency and decay rate, or attenuation, of these resonant modes are captured by the location and width of spectral peaks in the fracture transfer function, as we demonstrate shortly.

Krauklis waves

Before discussing the fracture transfer function, we review some key properties of Krauklis waves. This is most easily done in the context of an infinitely long fracture or fluid layer (with the constant initial width w_0) between identical elastic half-spaces. Seeking $e^{i(kx-\omega t)}$ solutions to the governing equations, and neglecting inertia of the solid (which is negligible for Krauklis waves at the low frequencies of interest to us), leads to the dispersion relation (Lipovsky and Dunham, 2015)

$$D_K(k,\omega) = \left(\frac{\tan\,\xi}{\xi} - 1\right)\left(\frac{c_0 k}{\omega}\right)^2 + 1 + \frac{2K}{G^* k w_0} = 0, \quad (8)$$

where $\xi = \sqrt{-i w_0^2 \omega/4\nu}$, $\nu = \mu/\rho$ is the fluid kinematic viscosity, k is the wavenumber, and ω is the angular frequency. Using the full linearized Navier-Stokes equation for the fluid and retaining inertia in the solid give rises to a more complex dispersion relation (Ferrazzini and Aki, 1987; Korneev, 2008) that has fundamental and higher mode solutions. In contrast, our approximate fluid model only captures the fundamental mode. However, the higher modes exist only above specific cutoff frequencies that are well outside the frequency range of interest. Here, we first discuss solutions to equation 8 for real ω and complex k. The spatial attenuation of the modes is quantified by

$$\frac{1}{2Q} = \frac{\mathrm{Im}\,k}{\mathrm{Re}\,k}, \quad (9)$$

where Q is the quality factor, approximately the number of spatial oscillations required for an appreciable decay of the amplitude. Plots of the phase velocity and attenuation are presented in Figure 3.

At high frequency (but still sufficiently low frequency as to justify the $\omega w_0/c_0 \ll 1$ approximation), the phase velocity approaches the fluid sound speed because the fracture walls are effectively rigid relative to the compressibility of the fluid. At frequencies below

$$f_{\mathrm{el}} = \frac{\omega_{\mathrm{el}}}{2\pi} = \frac{K c_0}{\pi G^* w_0}, \quad (10)$$

the elastic wall deformation becomes appreciable. This additional compliance leads to reduced phase velocity, given approximately as (Krauklis, 1962)

$$c \approx \left(\frac{G^* w_0 \omega}{2\rho}\right)^{1/3}. \quad (11)$$

Lower frequency waves propagate slower than higher frequency waves because the elastic walls are more compliant at longer wavelengths. Viscous dissipation is confined to thin boundary layers around the fracture walls.

At even lower frequencies, below

$$f_{\mathrm{vis}} = \frac{\omega_{\mathrm{vis}}}{2\pi} = \frac{2\mu}{\pi\rho w_0^2}, \quad (12)$$

Table 1. Material properties.

Solid (rock)	
Density ρ_s (kg/m^3)	2489
P-wave speed c_p (m/s)	4367
S-wave speed c_s (m/s)	2646
Fluid (water)	
Density ρ_0 (kg/m^3)	1000
Sound wave speed c_0 (m/s)	1500
Viscosity μ (Pa.s)	0.001

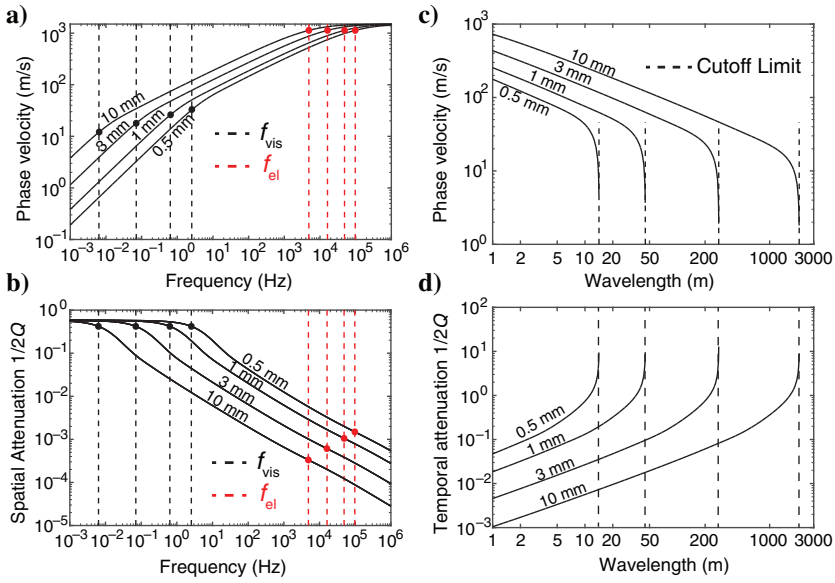

Figure 3. (a) Phase velocity and (b) spatial attenuation of Krauklis waves for a real frequency. (c) Phase velocity and (d) temporal attenuation for a real wavelength. Dispersion and attenuation curves are plotted for four fracture widths: 0.5, 1, 3, and 10 mm, as labeled. The dashed black and red lines in (a and b) mark the characteristic frequencies f_{vis} and f_{el} defined in the text. Dashed lines in (c and d) mark the cutoff wavelength λ_c, beyond which waves cease to propagate.

viscous effects are felt across the entire width of the fluid layer and the velocity v approaches the well-known parabolic Poiseuille flow profile. Viscous dissipation is sufficiently severe as to damp out waves over only a few cycles of oscillation; in addition, phase velocity decreases below that given in equation 11.

An important consequence of dissipation, from the viscous effects and from elastic-wave radiation, is that Krauklis-wave resonance will only occur in sufficiently short fractures. We can gain deeper insight by plotting the phase velocity and attenuation of Krauklis waves for real wavelength λ and complex frequency in Figure 3c and 3d, which correspond to standing waves formed by pairs of counterpropagating Krauklis waves. The temporal attenuation is quantified by

$$\frac{1}{2Q} = \frac{\mathrm{Im}\,\omega}{\mathrm{Re}\,\omega}, \tag{13}$$

for temporal quality factor Q. When the wavelength exceeds a cutoff wavelength (Lipovsky and Dunham, 2015)

$$\lambda_c = 2\pi\left(\frac{60\mu^2}{G^*\rho w_0^5}\right)^{-1/3}, \tag{14}$$

the phase velocity drops to zero and temporal attenuation diverges. This expression, corresponding to the dashed lines in Figure 3c and 3d, provides a crude estimate of the maximum length of fractures that can exhibit resonant oscillations. However, it is essential to account for additional dissipation that occurs from the decreased width near the fracture tip, and this is best done numerically. We therefore quantify the detectability limits of the fractures, using our 2D plane-strain simulations, in a later section.

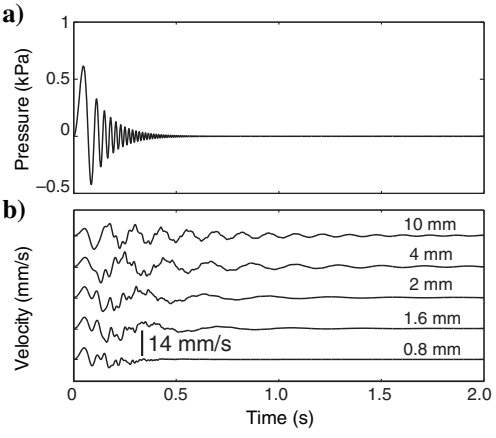

Figure 4. Response of fractures to (a) broadband pressure chirp at the fracture mouth, quantified through (b) width-averaged velocity at the fracture mouth. The response, shown for five fractures having the same length ($L = 10$ m) and different widths (the value given above each curve), is characterized by several resonance frequencies. The resonance frequency decreases as the width decreases, as anticipated from the dependence of the Krauklis-wave phase velocity on the width (equation 11 and Figure 3a). Higher frequencies decay quickly, leaving only the fundamental resonant mode. Wider fractures experience less viscous dissipation (Figure 3b), and hence they oscillate longer.

Fracture transfer function

Now, we turn our attention to finite-length fractures. Our objective is to quantify the response of the fracture to forcing at the fracture mouth, where the fracture connects to the wellbore. This is done through the dimensionless fracture transfer function $F(\omega)$ that relates pressure $p(0,t)$ and width-averaged velocity $u(0,t)$ at the fracture mouth:

$$\hat{u}(0,\omega) = \frac{F(\omega)}{\rho c_0}\hat{p}(0,\omega), \tag{15}$$

where $\hat{u}(0,\omega)$ and $\hat{p}(0,\omega)$ are the Fourier transform of width-averaged velocity and pressure, respectively. The fracture transfer function is related to the more commonly used fracture hydraulic impedance $Z_f(\omega)$ defined in equation 1 by

$$F(\omega) = \frac{\rho c_0/A_f}{Z_f(\omega)}, \tag{16}$$

where A_f is the cross-sectional area of the fracture mouth. We have nondimensionalized $F(\omega)$ using the fluid acoustic impedance ρc_0, such that $F(\omega) = 1$ for an infinitely long layer of inviscid, compressible fluid between parallel, rigid walls.

To calculate the fracture transfer function, numerical simulations such as that in Figure 2 are performed by imposing the pressure at the fracture mouth $p(0,t)$ and measuring the resulting width-averaged velocity at the fracture mouth $u(0,t)$. Figure 4 illustrates the sensitivity of $u(0,t)$ to the fracture geometry, given the same chirp input $p(0,t)$.

Then, $p(0,t)$ and $u(0,t)$ are Fourier transformed and the fracture transfer function is calculated using equation 15. An example is shown in Figure 5. Figure 6 compares the amplitude of the transfer function $|F|$ for fractures of different lengths and widths. The transfer functions exhibit multiple spectral peaks, corresponding to the resonant modes of the fracture (with a constant pressure boundary condition at the fracture mouth). These peaks are finite because of dissipation from viscosity and seismic radiation. Longer and narrower fractures have lower resonance frequencies, which is due to higher compliance and slower Krauklis-wave phase velocities.

We next examine the asymptotic behavior of the fracture transfer function at low frequencies, which facilitates comparison with quasi-static fracture models that have been widely used in the literature on hydraulic impedance testing and fracture diagnostics using water-hammer signals (Holzhausen and Gooch, 1985a, 1985b; Holzhausen and Egan, 1986; Paige et al., 1995; Mondal, 2010; Carey et al., 2015). By low frequency, we mean $\omega \ll c(\omega)/L$, where $c(\omega)$ is the Krauklis-wave phase velocity and L is the fracture length. Using equation 11 for $c(\omega)$, the low-frequency condition is $\omega \ll (G^* w_0 L^3/2\rho)^{1/2}$ or $\omega/2\pi \ll 15$ Hz for $L \sim 1$ m and $w_0 \sim 1$ mm. The low-frequency condition results in effectively uniform pressure across the length of the crack (at least when viscous pressure losses can be neglected) and the fracture response can be described by a much simpler model. The global mass balance for the fracture, within the context of our linearization, is

$$w_0 u(0,t) \approx \frac{d}{dt}\int_0^L w(x,t)dx, \tag{17}$$

where we have assumed that the fluid is effectively incompressible at these low frequencies, such that inflow of fluid (the left side) is bal-

anced by changes in width (the right side). Given that the fracture is very thin and approximately planar, the change in the opening is then related to the pressure change using the well-known solution for a plane strain mode I crack in an infinite medium (Lawn, 1993). The result is

$$u(0,t) \approx \frac{\pi L^2}{4w_0 G^*}\frac{dp}{dt}. \tag{18}$$

It follows, upon Fourier transforming equation 18 and using equation 15, that

$$F(\omega) \approx \frac{-i\pi L^2 \rho c_0}{4G^* w_0}\omega \quad \text{as} \quad \omega \to 0. \tag{19}$$

This asymptotic behavior is essentially the same as that quantified by Holzhausen and Gooch (1985a) as the fracture capacitance, although our result is for the 2D plane strain case to permit comparison with our simulations.

The low-frequency asymptotes (equation 19) are plotted as dashed lines in Figures 5a (inset) and 6, verifying that our numerical simulations accurately capture the quasi-static response. However, this asymptotic behavior only applies in the extreme low-frequency limit (far below the first resonance frequency) and deviates substantially from the actual response at higher frequencies. The traditional hydraulic impedance testing method (Holzhausen and Gooch, 1985a; Holzhausen and Egan, 1986) thus leaves the vast spectrum at higher frequencies unexplored.

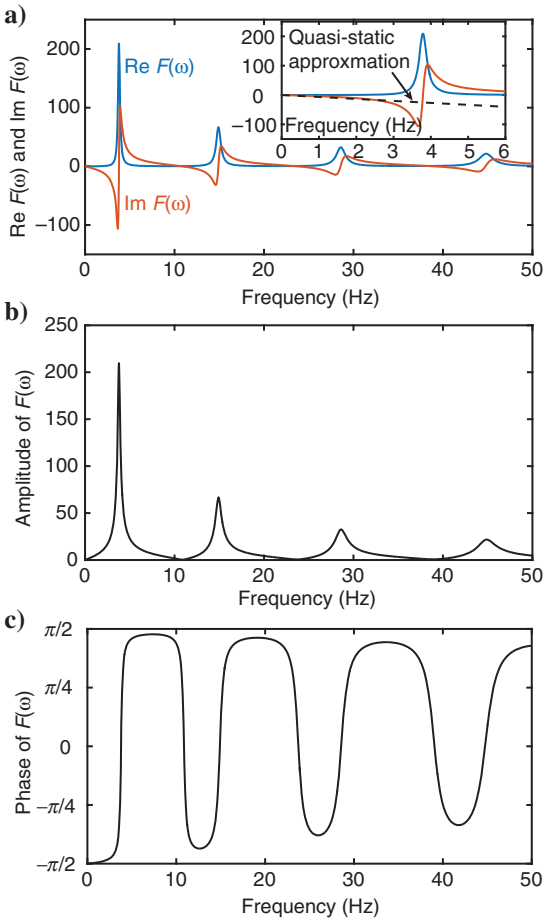

Figure 5. Fracture transfer function $F(\omega)$ for a 10 m long fracture of 5 mm width at the fracture mouth and the profile shown in Figure 6a. (a) Real and imaginary parts of $F(\omega)$. Inset shows low-frequency response, which is compared with the quasi-static approximation (equation 19) used in hydraulic impedance testing. Also shown are the (b) amplitude and (c) phase of $F(\omega)$.

We also derive an approximate analytical solution to the transfer function based on the dispersion relation (rather than using simulations). This dispersion-based approach has been used in several studies (Hornby et al., 1989; Kostek et al., 1998a; Henry, 2005; Derov et al., 2009), and it is illustrative to compare it with the more rigorous simulation-based solution. The solution, derived in Appendix A, assumes uniform width and imposes a zero-velocity boundary condition at the fracture tip. The resulting fracture transfer function is

$$F(\omega) = \frac{-ik(\omega)c_0 \tan[k(\omega)L]}{\omega}, \tag{20}$$

where $k(\omega)$ is the complex wavenumber obtained by solving the dispersion equation 8, assuming real angular frequency ω.

Our numerical simulations permit an exploration of how the decreased width near the fracture tip alters the fracture response, relative to the more idealized models based on dispersion (equation 20) that assume tabular (uniform-width) fractures. Figure 7 compares transfer functions for 1 m long fractures with the same width (2 mm) at the fracture mouth but different profiles near the tip. These range from a

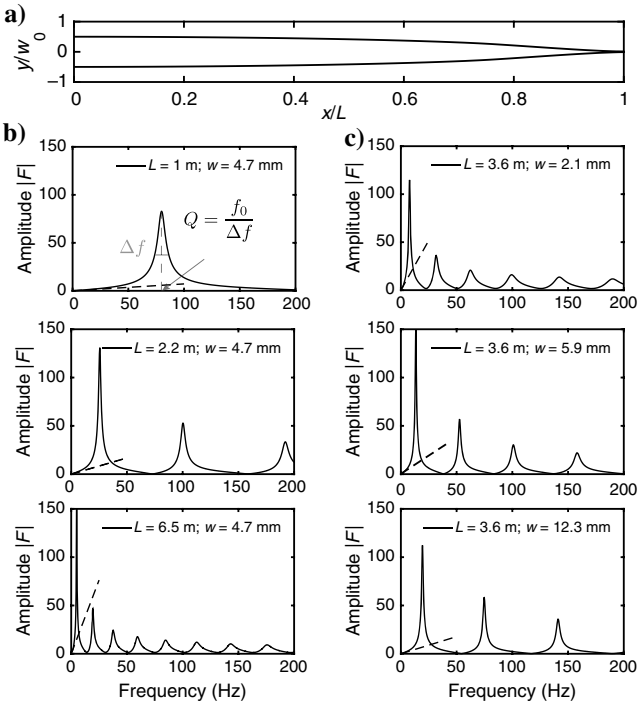

Figure 6. Fracture transfer functions for different fracture lengths and widths. (a) Normalized fracture geometry with the fracture tip width equal to 1/50 of the width at the fracture mouth. (b) Fracture transfer functions for 4.7 mm wide fractures with varied lengths. Longer fractures have lower resonance frequencies. (c) Fracture transfer functions for 3.6 m long fractures with varied widths. Wider fractures have higher resonance frequencies. In panels (b and c), the dashed lines plot the quasi-static limit (equation 19).

tabular fracture to ones in which the width at the tip is decreased to only 1/50 of the maximum width. As the fracture tip width is reduced, the resonance frequencies and the fracture transfer function amplitude at resonance peaks are shifted to lower values. This is due to higher viscous dissipation and slower Krauklis-wave phase velocity for narrower fractures. The differences are most pronounced at higher frequencies and for higher resonant modes. This finding highlights the importance of accounting for the near-tip geometry when using high-frequency data to determine fracture geometry. The tabular or flat fracture model (equation 20) can lead to substantial errors; in this example, there is approximately 20% error in the fundamental frequency and 100% error in the amplitude of the fundamental mode spectral peak.

Fracture geometry inference and detectability limits

As evidenced in Figures 4–7, the fracture response, as embodied by the fracture transfer function, is sensitive to fracture geometry (length and width). We now consider the inverse problem, that is, determining the fracture geometry from properties of the resonant modes of the fracture. Lipovsky and Dunham (2015), building on work by Korneev (2008) and Tary et al. (2014), show how measurements of the resonance frequencies and attenuation or decay rates associated with resonant modes could be used to uniquely determine the length and width. Their work uses dispersion relations derived for harmonic waves in an infinitely long fluid layer, and we have seen, in Figure 7, some notable discrepancies as compared with our numerical simulations of finite-length fractures. We thus revisit this problem, focusing in particular on the detectability limits.

As the fracture length grows, the resonance wavelengths increase and eventually reach a cutoff limit, beyond which the temporal attenuation diverges (Figure 3d). This provides the most optimistic estimate of fracture detectability using resonance; noise in real measurements will further limit the detectability.

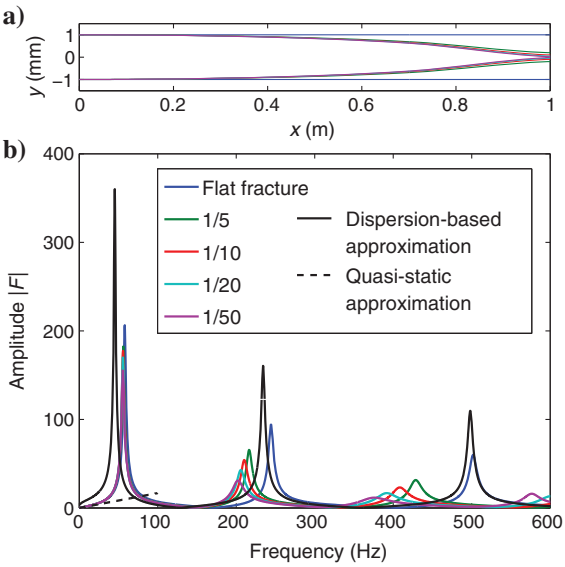

Figure 7. (a) Geometry of a 1 m long fracture with the tip width varied from 1, 1/5, 1/20, to 1/50 of the width at the fracture mouth (2 mm). (b) Amplitude of the fracture transfer function with varied fracture tip width compared with the dispersion-based approximation solution (equation 20) and the quasi-static limit (equation 19).

Figure 8a shows a graphical method for estimating fracture geometry from measurements of the frequency and temporal quality factor Q of the fundamental mode. This is similar to Figures 6–8 in Lipovsky and Dunham (2015), but here the fundamental mode properties are determined from transfer functions from numerical simulations using the tapered fracture shape shown in Figure 6a. Specifically, $Q = f_0/\Delta f$ for fundamental frequency f_0 and Δf, the full width at half of the maximum amplitude in a plot of $|F|$ (Figure 6b). We also provide, in Figure 8b and 8c, a comparison between our numerical results (for a tapered width) and predictions based on the dispersion relation (for a uniform width). Note that the dispersion solutions are calculated for zero velocity at the fracture tip and constant pressure at the fracture mouth, whereas Lipovsky and Dunham (2015) assume zero velocity at both tips. Viscous dissipation is underestimated using the dispersion-based approach, which ignores the narrow region near the fracture tip. There are also differences in the resonance frequency; the finite-length fractures in our numerical simulations are stiffer, and hence they resonate at higher frequencies, than those suggested by the dispersion-based method.

We finish this section by noting that quantitative results in Figure 8 are specific to the 2D plane strain problem. We anticipate that an axisymmetric (penny-shaped) fracture would have a similar response, but we caution that these results are unlikely to apply to 3D fractures when the length greatly exceeds the height. That case, which is of great relevance to the oil and gas industry, warrants study using 3D numerical simulations.

TUBE-WAVE INTERACTION WITH FLUID-FILLED FRACTURES

Having focused on the fracture response in the previous sections, we now return to the overall problem of determining the response of the coupled wellbore-fracture system. We present a simple model for low-frequency tube waves, and we derive reflection/transmission coefficients that quantify tube-wave interaction with a fracture intersecting the wellbore. We then examine the system response to excitation at the wellhead or at one end of a sealed interval, noting the possibility of a matched resonance between tube waves in the wellbore and Krauklis waves in the fracture.

Tube-wave governing equations and wellbore-fracture coupling

Let z be the distance along the well. The wellbore, with a constant radius a and cross-sectional area $A_T = \pi a^2$, is intersected by a fracture at $z = 0$ with aperture w_0 at the fracture mouth. Low-frequency tube waves are governed by the linearized momentum and mass balance equations (and the latter is combined with linearized constitutive laws for a compressible fluid and deformable elastic solid surrounding the wellbore):

$$\frac{\rho}{A_T}\frac{\partial q}{\partial t} + \frac{\partial p}{\partial z} = 0, \tag{21}$$

$$\frac{A_T}{M}\frac{\partial p}{\partial t} + \frac{\partial q}{\partial z} = -A_f u(t)\delta(z), \tag{22}$$

where $q(z,t)$ is the volumetric flow rate along the wellbore, $p(z,t)$ is the pressure, $u(t)$ is the velocity into the fracture at the fracture

mouth, ρ is the fluid density (assumed to be the same as in the fracture), M is a modulus that is typically close to the fluid bulk modulus (Biot, 1952), and A_f is the fracture mouth area. For a fracture intersecting the wellbore perpendicularly, as we assume in the examples presented below, $A_f = 2\pi a w_0$. This can be generalized to account for fractures intersecting the wellbore at other angles (Hornby et al., 1989; Derov et al., 2009). These equations describe nondispersive wave propagation at the tube-wave speed $c_T = \sqrt{M/\rho}$, which we solve in the frequency domain using Fourier transforms. However, they could also be solved by a time-domain finite-difference method (Liang et al., 2015; Karlstrom and Dunham, 2016) or by the method of characteristics (Mondal, 2010; Carey et al., 2015), both of which permit spatial variation of properties. In all examples shown below, we set the wellbore diameter to $2a = 0.1$ m and assume $M = K$ (and hence $c_T = c_0$) for simplicity, although expressions are given for the general case. The model can, of course, be generalized to account for permeable walls (Tang, 1990), irregularly shaped boreholes (Tezuka et al., 1997), spatially variable properties (Chen et al., 1996; Wang et al., 2008), and friction (Livescu et al., 2016). The source term on the right side of the mass balance equation 22 describes the mass exchange between the wellbore and the fracture at the fracture mouth. Because the fracture aperture is much smaller than the tube-wave wavelength, the source term is approximately a delta function at the fracture location.

Integrating equations 21 and 22 across the junction at the wellbore-fracture intersection, we obtain the following jump conditions:

$$q(0^+, t) - q(0^-, t) = -A_f u(t), \tag{23}$$

$$p(0^+, t) - p(0^-, t) = 0. \tag{24}$$

The pressure is continuous across the junction, whereas the volumetric flow rate (and fluid particle velocity through the wellbore) experiences a jump that accounts for mass exchange with the fracture. The volumetric flow rate into the fracture $A_f u(t)$ is related to the pressure at the fracture mouth $p(0, t)$ through the fracture transfer function using equation 15 (or, equivalently, the fracture hydraulic impedance $Z_f(\omega)$). Although we focus on one intersecting fracture in this study, extension to multiple fractures is straightforward by adding multiple jump conditions similar to equations 23 and 24. By Fourier transforming equations 23 and 24 and using equation 15, we obtain

$$\hat{q}(0^+,\omega) - \hat{q}(0^-,\omega) = -\frac{A_f F(\omega)}{\rho c_0}\hat{p}(0,\omega) = -\frac{\hat{p}(0,\omega)}{Z_f(\omega)}. \tag{25}$$

Tube-wave reflection/transmission coefficients

We now derive the reflection and transmission coefficients of tube waves incident on the fracture. Assuming an infinitely long well, we seek a Fourier-domain solution of the form:

$$\hat{p}(z,\omega) = \begin{cases} e^{ikz} + \mathrm{R}e^{-ikz}, & z < 0, \\ Te^{ikz}, & z > 0, \end{cases} \tag{26}$$

where $k = \omega/c_T$ is the wavenumber, the incident wave has unit amplitude, and R and T are the reflection and transmission coefficients, respectively. Satisfying the governing equations 21 and 22 and the fracture junction conditions (equations 24 and 25) yields

$$R(\omega) = -\frac{r(\omega)/2}{1 + r(\omega)/2} = -\frac{1}{1 + 2/r(\omega)}, \tag{27}$$

$$T(\omega) = \frac{1}{1 + r(\omega)/2} = \frac{2/r(\omega)}{1 + 2/r(\omega)}, \tag{28}$$

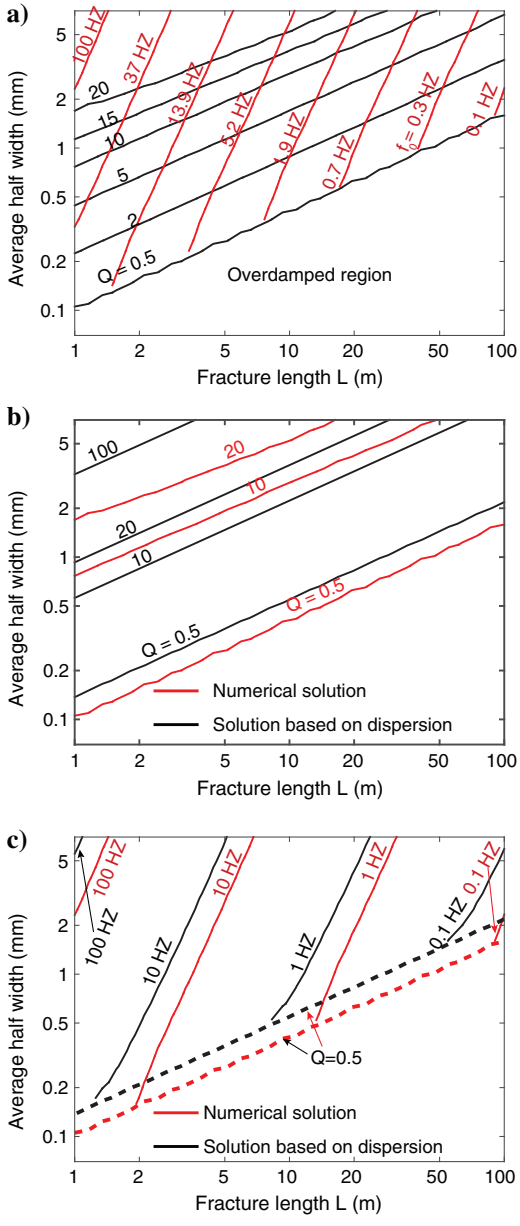

Figure 8. (a) Graphical method to determine the fracture length and width from frequency (red curves) and temporal quality factor Q (black curves) of the fundamental resonant mode (i.e., from the fracture transfer function from numerical simulations using the tapered fracture geometry; see Figure 6). In the overdamped region ($Q < 0.5$), viscous dissipation prevents resonant oscillations and the geometry cannot be determined with this method. (b) Quality factor and (c) frequency, comparing numerical simulation results with solutions based on the dispersion relation (equation 8).

in which

$$r(\omega) = \frac{Z_T}{Z_f(\omega)} = \frac{\rho c_T / A_T}{\rho c_0 / A_f} F(\omega) \tag{29}$$

is the ratio of the hydraulic impedance of tube waves in the wellbore, $Z_T \equiv \rho c_T / A_T$, to the fracture hydraulic impedance $Z_f(\omega)$. The factor of two in the expressions for $R(\omega)$ and $T(\omega)$ arises because a pair of tube waves propagate away from the fracture.

Figure 9 explores the relation between the fracture transfer function and the reflection/transmission coefficients. The maximum reflection approximately coincides with the resonance peaks in the transfer functions, corresponding to the eigenmodes of the fracture with a constant pressure boundary condition at the fracture mouth. At these frequencies, the hydraulic impedance of the fracture is much smaller than that of tube waves (i.e., $r(\omega)/2 \gg 1$), and only small pressure changes at the fracture mouth are required to induce a large flow into or out of the fracture. The reflection coefficient goes to -1 in this limit, so that waves at these specific frequencies are reflected as if from a constant pressure boundary. We also note that reducing the fracture width decreases reflection because the fracture mouth area decreases relative to the wellbore cross-sectional area A_T and because the fracture resonance peak amplitude decreases due to increased viscous dissipation in narrower fractures (captured in F or Z_f).

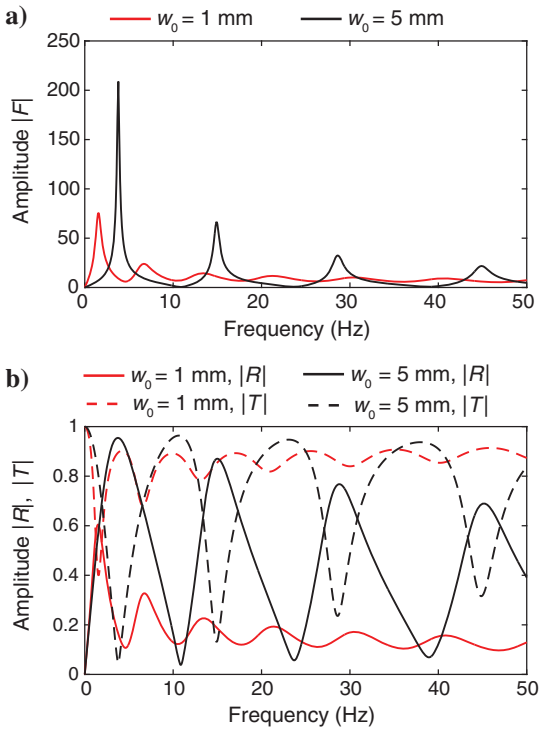

Figure 9. (a) Amplitude of the fracture transfer functions $|F|$ for two 10 m long fractures with different widths (1 and 5 mm). (b) Amplitude of the tube-wave reflection and transmission coefficients, $|R|$ and $|T|$, across the fracture (equations 27 and 28) for the wellbore diameter $2a = 0.1$ m. Maximum reflection occurs at the resonance frequencies of the fracture.

Response of the wellbore-fracture system

We now consider a finite-length section of the well intersected by a single fracture, with boundary conditions prescribed at both ends of the well section. These ends might coincide with the wellhead and well bottom or the two ends of a sealed interval. Let h_1 and h_2 be the lengths of the two sections above and below the fracture, respectively, with the fracture at $z = 0$ as before. We seek the pressure and velocity within the wellbore, given some excitation at the end of the upper well section.

Equations 21 and 22 are supplemented with boundary conditions at the top and bottom of the wellbore. At the top ($z = -h_1$), we set the volumetric flow rate into the well equal to a prescribed injection rate $Q(t)$, not to be confused with the quality factor discussed earlier:

$$q(-h_1, t) = Q(t). \tag{30}$$

In Appendix B, we show that this boundary condition is mathematically equivalent to the case of a sealed end (i.e., $q(-h_1, t) = 0$) with a monopole source placed within the wellbore just below the end. At the bottom ($z = h_2$), we assume a partially reflecting condition of the form

$$p(h_2, t) - Z_T q(h_2, t) = R_b[p(h_2, t) + Z_T q(h_2, t)], \tag{31}$$

in which R_b is the well bottom reflection coefficient (satisfying $|R_b| \le 1$). This boundary condition can be equivalently written in terms of the hydraulic impedance Z_b at the bottom of the well:

$$p(h_2, t) = Z_b q(h_2, t), Z_b = \frac{1 + R_b}{1 - R_b} Z_T. \tag{32}$$

We assume constant, real R_b (and hence Z_b), although it is possible to use a frequency-dependent, complex-valued R_b if desired. For $R_b = 0$, there is no reflection from the bottom, $R_b = 1$ corresponds to $q(h_2, t) = 0$, and $R_b = -1$ corresponds to $p(h_2, t) = 0$.

The solution to the stated problem is

$$\hat{p}(z,\omega) = \begin{cases} a_1 \sin(kz) + a_2 \cos(kz), & -h_1 < z < 0, \\ b_1 e^{ikz} + b_2 e^{-ikz}, & 0 < z < h_2, \end{cases} \tag{33}$$

$$Z_T \hat{q}(z,\omega) = \begin{cases} -ia_1 \cos(kz) + ia_2 \sin(kz), & -h_1 < z < 0, \\ b_1 e^{ikz} - b_2 e^{-ikz}, & 0 < z < h_2, \end{cases} \tag{34}$$

where $k = \omega / c_T$ and the coefficients a_1, a_2, b_1, and b_2 are determined by the top boundary condition (equation 30), bottom boundary condition (equation 31), and fracture junction conditions (equations 24 and 25):

$$a_1 = \frac{iZ_T \hat{Q}(\omega)}{D(\omega)}, \tag{35}$$

$$a_2 = \frac{Z_T \hat{Q}(\omega)}{[r(\omega) + \Lambda(\omega)] D(\omega)}, \tag{36}$$

$$b_1 = \frac{Z_T \hat{Q}(\omega)}{(1 + R_b e^{2ikh_2})[r(\omega) + \Lambda(\omega)]D(\omega)}, \quad (37)$$

$$b_2 = \frac{R_b e^{2ikh_2} Z_T \hat{Q}(\omega)}{(1 + R_b e^{2ikh_2})[r(\omega) + \Lambda(\omega)]D(\omega)}, \quad (38)$$

where

$$D(\omega) = \cos(kh_1) - \frac{i \sin(kh_1)}{r(\omega) + \Lambda(\omega)}, \quad (39)$$

$$\Lambda(\omega) = \frac{1 - R_b e^{2ikh_2}}{1 + R_b e^{2ikh_2}}, \quad (40)$$

and $r(\omega)$ is the hydraulic impedance ratio defined as before (equation 29). Solutions in the time domain are obtained by inverting the Fourier transform.

Excitation at the wellhead

Here, we use the solution derived above to demonstrate how fracture growth might be monitored using tube waves or water-hammer signals generated by excitation at the wellhead. The wellbore has a total length of 3 km, a diameter of $2a = 0.1$ m, and a partially sealed bottom with reflection coefficient $R_b = 0.8$. A single fracture is placed 2 km from the wellhead and 1 km from the well bottom (i.e., $h_1 = 2$ km and $h_2 = 1$ km). At the wellhead, we prescribe a broadband chirp (up to approximately 500 Hz) in velocity, as shown in Figure 10. As mentioned earlier and detailed in Appendix B, this is equivalent to placing a monopole source a short distance below the sealed wellhead. Pressure perturbations could be generated by abruptly shutting in the well, as is done in hydraulic impedance testing (Holzhausen and Egan, 1986; Carey et al., 2015). However, an engineered source would provide better control over the source spectrum. To account for dissipation during tube-wave propagation along the wellbore, we add a small imaginary part to the tube-wave speed: $c_T = (1 - 10^{-3}i)\sqrt{M/\rho}$. Figure 11 shows a schematic of this system and the synthetic borehole record section. The interplay between tube waves in the wellbore and dispersive Krauklis waves within the fracture is evident.

Matched resonance

The example shown in Figure 11 illustrates the response when the entire long wellbore is hydraulically connected to the fracture. Distinct reflections can be seen, and interference between different reflections is confined to short time intervals. We next examine the more complex response that arises when a much smaller section of the well around the fracture is sealed at both ends and a source is placed at one end. The solution given in equations 33–40 still applies, but we select a smaller length h_1. There is now complex interference between multiply reflected waves; whether this interference is constructive or destructive depends on the well section lengths h_1 and h_2 and the fracture reflection/transmission coefficients (and hence frequency). As we demonstrate, the signals in

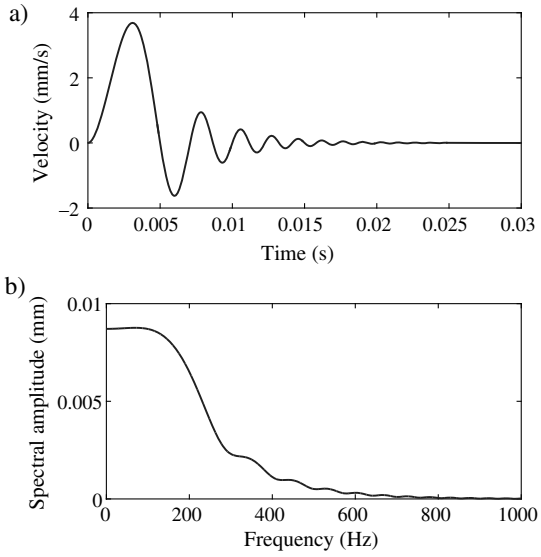

Figure 10. Chirp used for examples shown in Figures 11 and 12: (a) time series and (b) spectrum.

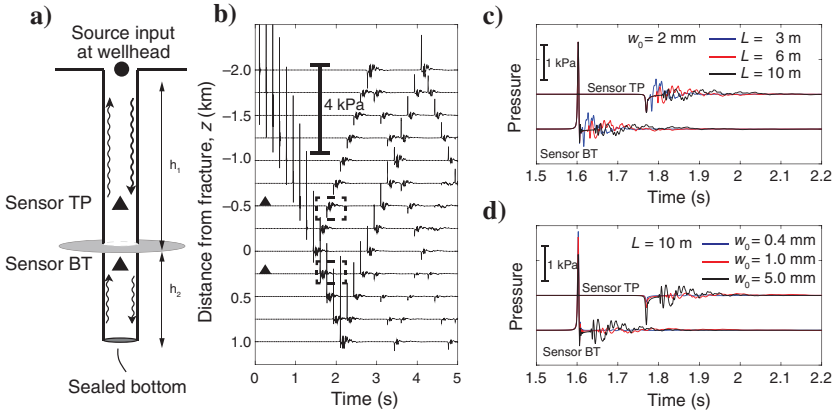

Figure 11. Response of the wellbore-fracture system to chirp excitation (Figure 10) at the wellhead. (a) Schematic of the system, with one fracture 2 km below the wellhead and 1 km above the well bottom. Sensor TP is 500 m above the fracture, and sensor BT is 250 m below the fracture. (b) Record section of pressure along the wellbore (every 250 m) with a fracture that is 10 m long and 2 mm wide at the fracture mouth. Multiple reflections from the fracture, well bottom, and wellhead are observed. Dashed boxes mark the time window (1.5–2.2 s) examined in panels (c and d) for sensors TP and BT. (c) Comparison of pressure at sensors TP and BT for fractures with the same width but different lengths. (d) Same as panel (c) but for fractures with the same length but different widths. In panels (c and d), sensor TP shows waves reflected from the fracture; first arriving are direct tube-wave reflections from the fracture mouth, followed by tube waves generated by Krauklis waves in the fracture that have reflected from the fracture tip. Sensor BT shows transmitted waves, which have similar arrivals. Longer fractures show a more dispersed set of Krauklis-wave arrivals. Reflections are smaller from narrower fractures.

the upper well section that contains the source can be selectively amplified when a resonance frequency of the upper well section is tuned to one of the resonance frequencies of the fracture. We refer to this phenomenon as matched resonance.

Reflection of waves from the fracture is most pronounced at frequencies that permit maximum exchange of fluid between the wellbore and fracture. These frequencies correspond approximately to the resonance frequencies of the fracture with a constant pressure boundary condition at the fracture mouth (i.e., corresponding to the peaks of the fracture transfer function; see Figure 9). The resonance frequencies of the upper wellbore section with a sealed top end

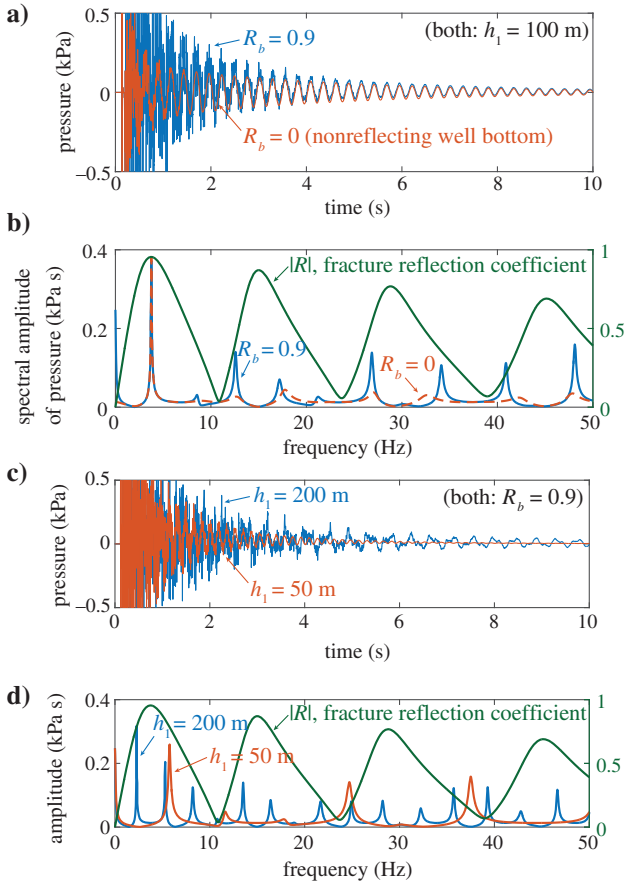

Figure 12. Matched resonance: The length of the upper wellbore section containing the source is chosen so that the resonance frequency of tube waves in this wellbore section matches the fundamental mode resonance frequency of the fracture (3.8 Hz). (a) Pressure response at a receiver in the center of the upper wellbore section (at $z = -h_1/2$) to the chirp excitation shown in Figure 10. The 3.8 Hz resonance is selectively amplified, regardless of the length of the lower wellbore section and the bottom boundary condition: Compare the case with a nonreflecting well bottom (red, $R_b = 0$) to partially sealed (blue, $R_b = 0.9$ and $h_2 = 10$ m). (b) Fourier amplitude spectrum of pressure time series shown in (a), with prominent peak at the 3.8 Hz matched resonance frequency. Although additional spectral peaks appear for the sealed bottom case, the matched resonance peak is nearly identical to the nonreflecting bottom case. Also, shown is the reflection coefficient of tube waves from the fracture, which has peaks at the fracture resonance frequencies. (c) Same as panel (a) but for $h_1 = 200$ and 50 m (with $R_b = 0.9$ and $h_2 = 10$ m). The system does not satisfy the matched resonance condition and the spectrum, shown in panel (d), is more complicated and lacks the pronounced peak at the fundamental resonance mode.

($q = 0$) and constant pressure condition ($p = 0$) at the fracture satisfy $\cos(\omega h_1/c_T) = 0$. For example, the lowest resonance frequency is $f = \omega/2\pi = c_T/4h_1$. Matched resonance occurs when one of these frequencies matches a fracture resonance frequency.

To justify this more rigorously, and explain some possible complications, we note that the tube-wave eigenfunctions associated with this resonant wellbore response are $\sin(\omega z/c_T)$, corresponding to the first term on the right side of equation 33. The amplitude of this term is given in equation 35, which is largest when the denominator $D(\omega)$, given in equation 39, is smallest. The hydraulic impedance ratio is quite large (ideally, $|r(\omega)| \gg 1$) around the fracture resonance frequencies. A further requirement is that $|\Lambda(\omega)|$ be sufficiently small compared with $|r(\omega)|$, at least around the targeted fracture resonance frequency. When these conditions are satisfied, $D(\omega) \approx \cos(kh_1)$ with $k = \omega/c_T$. Setting $D(\omega) = 0$ then yields the wellbore section resonance condition $\cos(\omega h_1/c_T) = 0$ stated above. Of course, this resonance condition is only an approximation, especially when $|r(\omega)|$ does not greatly exceed unity or when $|\Lambda(\omega)|$ is not small. In these cases, the matched resonance condition can be more precisely determined by finding the frequencies ω that minimize the exact $D(\omega)$ in equation 39. However, $\Lambda(\omega)$ can be made arbitrarily small by sealing the bottom end of the lower well section ($R_b = 1$ and hence $\Lambda(\omega) = -i\tan(\omega h_2/c_T)$) and decreasing h_2, such that $\omega h_2/c_T \ll 1$.

Figure 12a and 12b illustrates matched resonance. The frequency of the fundamental mode of the fracture (the 10 m long, 5 mm wide example shown in Figures 5 and 9) is $f \approx 3.8$ Hz, so the upper wellbore section is chosen to be $h_1 = 100$ m $\approx c_T/4f$ long to satisfy the matched resonance condition. The system is excited by a broadband chirp at the upper end of this wellbore section. The 3.8 Hz resonance frequency clearly dominates the system response. The response is shown for two bottom boundary conditions. The first is the relatively simple case of a well with a nonreflecting bottom boundary ($R_b = 0$, for which $\Lambda = 1$ regardless of h_2). This eliminates the possibility of resonance within the lower wellbore section and prevents bottom reflections from then transmitting through the fracture to return to the upper well section. The second case has $h_2 = 10$ m and $R_b = 0.9$, corresponding to a partially sealed end a short distance below the fracture. Although the initial response in the second case contains a complex set of high-frequency reverberations associated with reflections within the lower well section, these are eventually damped out to leave only the prominent 3.8 Hz resonance. This illustrates a rather remarkable insensitivity to characteristics of the lower well section because similar results (not shown) were found even for a wide range of lower well section lengths h_2.

We next demonstrate how changing the length of the upper well section h_1 alters the resonant response of the system. Figure 12c and 12d shows the responses for values of h_1 that are larger and smaller than the matched resonance length. The fundamental mode resonance peak shifts to a lower frequency when h_1 increases and to a higher frequency when h_1 decreases. Many resonant modes are excited for the large h_1 case, leading to a rather complex pressure response. The situation is simpler for the small h_1 case, but as h_1 continues to decrease, the amplitude of the fundamental mode peak continues to decrease and might be difficult to observe in noisy data.

Possible measuring techniques

Although it is easy to implement different excitation sources and receiver configurations in our theoretical calculations, it is not trivial

to make downhole pressure measurements in practice. In general, pressure is measured at the pump or in the pipe connecting the pump to the wellhead during hydraulic fracturing treatments. Installing downhole pressure transducers or hydrophones with complex pumping and treatment equipment in place during hydraulic fracturing would be challenging. In addition, downhole sensors can occupy a significant volume of the borehole and create complex tool effects on measured tube waves (Pardo et al., 2013). Quantifying such effects is beyond the scope of this study. A possible alternative approach would be to install geophones or pressure gauges in nearby monitoring wells. The model presented in this study would need to be extended to predict the signals in the monitoring wells, and it is uncertain if these signals would have as much useful information regarding the fracture geometry. Another technology that reduces the influence of the tool on tube-wave propagation is fiber-optic distributed acoustic sensing (DAS) (MacPhail et al., 2012; Molenaar et al., 2012; Boone et al., 2015). DAS cables can run through grooves across swellable packers along the casing in the sealing elements in uncemented packer and sleeve completion, and they can be buried in the cement in cemented plug-and-perf completions (Boone et al., 2015). This technology not only avoids any interaction with tube waves, but it can also provide continuous measurements along the full length of the wellbore.

CONCLUSION

We have investigated the interaction of tube waves with fractures. Although this problem has received much attention in the literature, previous work has been restricted to relatively idealized analytical or semianalytical models of the fracture response. In contrast, we advocate the use of numerical simulations to more accurately describe the fracture. These simulations account for variable fracture width, narrow viscous boundary layers adjacent to the fracture walls, and dissipation from viscosity and from seismic radiation. The simulations feature Krauklis waves propagating along the fracture; counterpropagating pairs of Krauklis waves form the eigenmodes of the fracture. As many authors note, the frequency and attenuation of these modes can be used to constrain fracture geometry.

Although this initial study uses a 2D plane strain fracture model, the overall methodology can be applied when 3D models of the fracture are available. Such models would permit investigation of fractures that have bounded height, a commonly arising situation in the industry, and one for which the 2D model presented here is not well-justified.

We then showed how to distill the simulation results into a single, complex-valued function that quantifies the fracture response, specifically its hydraulic impedance (or the normalized reciprocal of the impedance, the fracture transfer function). The fracture transfer function can then be used to determine how tube waves within a wellbore reflect and transmit from fractures intersecting the well, and to solve for the response of the wellbore-fracture system to excitation at the wellhead or within the wellbore.

The coupled wellbore-fracture system has a particularly complex response, potentially involving resonance within wellbore sections adjacent to the fracture or within the fracture itself. We found that it is possible to selectively amplify tube waves at the eigenfrequencies of the fracture by properly choosing the length of the well section containing the source and intersecting the fracture. This phenomenon, which we call matched resonance, could prove useful to excite and measure fracture eigenmodes, which can then be used to infer the fracture geometry.

ACKNOWLEDGMENTS

This work was supported by a gift from Baker Hughes to the Stanford Energy and Environment Affiliates Program and seed funding from the Stanford Natural Gas Initiative. O. O'Reilly was partially supported by the Chevron fellowship in the Department of Geophysics at Stanford University.

APPENDIX A

DISPERSION-BASED FRACTURE TRANSFER FUNCTION

In this appendix, we use the Krauklis-wave dispersion relation to derive an approximate expression for the fracture transfer function. Let x be the distance into the fracture measured from the fracture mouth at $x = 0$. The fracture has length L and uniform aperture w_0. Solutions in the frequency domain are written as a superposition of plane waves propagating in the $+x$ and $-x$ directions:

$$\hat{p}(x,\omega) = Ae^{ikx} + Be^{-ikx}, \tag{A-1}$$

$$\rho c\hat{u}(x,\omega) = Ae^{ikx} - Be^{-ikx}, \tag{A-2}$$

where $k = k(\omega)$ and $c = \omega/k(\omega)$ are the wavenumber and phase velocity determined by the Krauklis-wave dispersion relation (equation 8, solved for real ω and possibly complex k), and A and B are the coefficients determined by boundary conditions at the ends of the fracture. At the fracture tip, the fluid velocity is set to zero:

$$\rho c\hat{u}(L,\omega) = Ae^{ikL} - Be^{-ikL} = 0. \tag{A-3}$$

The fracture transfer function, defined in equation 15, is obtained by combining equations A-1–A-3:

$$F(\omega) = \frac{-ik(\omega)c_0 \tan[k(\omega)L]}{\omega}. \tag{A-4}$$

Peaks in $F(\omega)$ correspond to the resonance frequencies of the fracture with a constant pressure condition at the fracture mouth. Therefore, besides equation A-3, we have

$$\hat{p}(0,\omega) = A + B = 0. \tag{A-5}$$

Combining equations A-3 and A-5, we obtain the resonance condition

$$\cos kL = 0, \tag{A-6}$$

or $k_nL = (n - 1/2)\pi$ for positive integers $n = 1, 2, \ldots$. This can be solved, assuming a real k and a complex ω, for the resonance frequencies and (temporal) decay rates of the eigenmodes.

We next derive the resonance frequencies for the case of negligible dissipation (i.e., for an inviscid fluid). In this case, k and ω are real, and we have (Krauklis, 1962)

$$c(\omega) = (G^* w_0 \omega/2\rho)^{1/3} = (G^* w_0 \pi f/\rho)^{1/3}. \quad \text{(A-7)}$$

It follows that the resonance frequencies are

$$f_n = \sqrt{(\pi G^* w_0/\rho)[(n-1/2)/2L]^3}. \quad \text{(A-8)}$$

This expression provides a reasonably accurate prediction of the resonance frequencies for the examples shown in this work, provided that w_0 in equation A-8 is interpreted as average width.

APPENDIX B

EQUIVALENCE OF MONOPOLE SOURCE AND FLOW RATE BOUNDARY CONDITION

In this appendix, we establish the equivalence, for sufficiently low frequencies, between a monopole source placed just below the sealed end of a wellbore section and a prescribed flow rate boundary condition at that end. For convenience, we take $z = 0$ to coincide with the end. The tube-wave equations with a monopole source $m(t)$ at $z = s$ are

$$\frac{\rho}{A_T}\frac{\partial q}{\partial t} + \frac{\partial p}{\partial z} = 0, \quad \text{(B-1)}$$

$$\frac{A_T}{M}\frac{\partial p}{\partial t} + \frac{\partial q}{\partial z} = m(t)\delta(z-s). \quad \text{(B-2)}$$

For the sealed end, $q(0,t) = 0$, whereas the prescribed flow rate boundary condition is

$$q(0,t) = Q(t). \quad \text{(B-3)}$$

We now show equivalence of these two problems, in the sense that $Q(t) \approx m(t)$, for frequencies satisfying

$$s\omega/c_T \ll 1. \quad \text{(B-4)}$$

This is done by requiring that the outgoing waves below the source ($z > s$) are identical for the two problems.

The solution to equations B-1 and B-2 in a semi-infinite wellbore with a sealed end at $z = 0$ is

$$\hat{p}(z,\omega) = \begin{cases} a\cos(\omega z/c_T), & 0 < z < s, \\ be^{i\omega(z-s)/c_T}, & z > s, \end{cases} \quad \text{(B-5)}$$

$$Z_T\hat{q}(z,\omega) = \begin{cases} ia\sin(\omega z/c_T), & 0 < z < s \\ be^{i\omega(z-s)/c_T}, & z > s, \end{cases} \quad \text{(B-6)}$$

where a and b are the constants to be determined.

Fourier transforming equations B-1 and B-2 and integrating across the source yields the jump conditions across the source:

$$\hat{p}(s^+,\omega) - \hat{p}(s^-,\omega) = 0, \quad \text{(B-7)}$$

$$\hat{q}(s^+,\omega) - \hat{q}(s^-,\omega) = \hat{m}(\omega). \quad \text{(B-8)}$$

Constants a and b are determined by substituting equations B-5 and B-6 into equations B-7 and B-8:

$$a = Z_T\hat{m}(\omega)e^{is\omega/c_T}, \quad \text{(B-9)}$$

$$b = Z_T\hat{m}(\omega)\cos(s\omega/c_T)e^{is\omega/c_T}. \quad \text{(B-10)}$$

Substituting equations B-9 and B-10 into equations B-5 and B-6, we obtain the solution below the source ($z > s$):

$$\hat{p}(z,\omega) = Z_T\hat{m}(\omega)\cos(s\omega/c_T)e^{i\omega z/c_T}, \quad \text{(B-11)}$$

$$\hat{q}(z,\omega) = \hat{m}(\omega)\cos(s\omega/c_T)e^{i\omega z/c_T}. \quad \text{(B-12)}$$

Similarly, we obtain the solution to the tube-wave problem with no internal source but with the top boundary condition being $q(0,t) = Q(t)$:

$$\hat{p}(z,\omega) = Z_T\hat{Q}(\omega)e^{i\omega z/c}, \quad \text{(B-13)}$$

$$\hat{q}(z,\omega) = \hat{Q}(\omega)e^{i\omega z/c}. \quad \text{(B-14)}$$

We now determine the condition for which the wavefield below the source ($z > s$) is identical between the two problems. Specifically, we require the equivalence of equations B-11 and B-13 and similarly for equations B-12 and B-14. The necessary condition is

$$\hat{Q}(\omega) = \hat{m}(\omega)\cos(s\omega/c_T). \quad \text{(B-15)}$$

Moreover, for sources placed just below the sealed end, or equivalently at sufficiently low frequencies, $s\omega/c_T \ll 1$ and $\cos(s\omega/c_T) \approx 1$. Thus, $\hat{Q}(\omega) \approx \hat{m}(\omega)$ or $Q(t) \approx m(t)$, as claimed.

REFERENCES

Aki, K., M. Fehler, and S. Das, 1977, Source mechanism of volcanic tremor: Fluid-driven crack models and their application to the 1963 Kilauea eruption: Journal of Volcanology and Geothermal Research, **2**, 259–287, doi: 10.1016/0377-0273(77)90003-8.

Bakku, S. K., M. Fehler, and D. Burns, 2013, Fracture compliance estimation using borehole tube waves: Geophysics, **78**, no. 4, D249–D260, doi: 10.1190/geo2012-0521.1.

Batchelor, G. K., 2000, An introduction to fluid dynamics: Cambridge University Press.

Beydoun, W. B., C. H. Cheng, and M. N. Toksz, 1985, Detection of open fractures with vertical seismic profiling: Journal of Geophysical Research: Solid Earth, **90**, 4557–4566, doi: 10.1029/JB090iB06p04557.

Biot, M., 1952, Propagation of elastic waves in a cylindrical bore containing a fluid: Journal of Applied Physics, **23**, 997–1005, doi: 10.1063/1.1702365.

Boone, K., R. Crickmore, Z. Werdeg, C. Laing, and M. Molenaar, 2015, Monitoring hydraulic fracturing operations using fiber-optic distributed acoustic sensing: Presented at the Unconventional Resources Technology Conference (URTEC).

Candela, T., F. Renard, Y. Klinger, K. Mair, J. Schmittbuhl, and E. E. Brodsky, 2012, Roughness of fault surfaces over nine decades of length scales: Journal of Geophysical Research: Solid Earth, **117**, B08409, doi: 10.1029/2011JB009041.

Carey, M. A., S. Mondal, and M. M. Sharma, 2015, Analysis of water hammer signatures for fracture diagnostics: Presented at the SPE Annual Technical Conference and Exhibition.

Chen, X., Y. Quan, and J. M. Harris, 1996, Seismogram synthesis for radially layered media using the generalized reflection/transmission coefficients method: Theory and applications to acoustic logging: Geophysics, **61**, 1150–1159, doi: 10.1190/1.1444035.

Chen, Y., and L. Knopoff, 1986, Static shear crack with a zone of slip-weakening: Geophysical Journal International, **87**, 1005–1024, doi: 10.1111/j.1365-246X.1986.tb01980.x.

Chouet, B., 1986, Dynamics of a fluid-driven crack in three dimensions by the finite difference method: Journal of Geophysical Research: Solid Earth, **91**, 13967–13992.

Chouet, B., 1988, Resonance of a fluid-driven crack: Radiation properties and implications for the source of long-period events and harmonic tremor: Journal of Geophysical Research: Solid Earth, **93**, 4375–4400, doi: 10.1029/JB093iB05p04375.

Derov, A., G. Maximov, M. Lazarkov, B. Kashtan, and A. Bakulin, 2009, Characterizing hydraulic fractures using slow waves in the fracture and tube waves in the borehole: 79th Annual International Meeting, SEG, Expanded Abstracts, 4115–4119.

Dunham, E. M., D. Belanger, L. Cong, and J. E. Kozdon, 2011, Earthquake ruptures with strongly rate-weakening friction and off-fault plasticity. Part 2: Nonplanar faults: Bulletin of the Seismological Society of America, **101**, 2308–2322, doi: 10.1785/0120100076.

Dunham, E. M., and D. E. Ogden, 2012, Guided waves along fluid-filled cracks in elastic solids and instability at high flow rates: Journal of Applied Mechanics, **79**, 031020, doi: 10.1115/1.4005961.

Ferrazzini, V., and K. Aki, 1987, Slow waves trapped in a fluid-filled infinite crack: Implication for volcanic tremor: Journal of Geophysical Research: Solid Earth, **92**, 9215–9223.

Frehner, M., 2013, Krauklis wave initiation in fluid-filled fractures by seismic body waves: Geophysics, **79**, no. 1, T27–T35, doi: 10.1190/geo2013-0093.1.

Frehner, M., and S. M. Schmalholz, 2010, Finite-element simulations of Stoneley guided-wave reflection and scattering at the tips of fluid-filled fractures: Geophysics, **75**, no. 2, T23–T36, doi: 10.1190/1.3340361.

Henry, F., 2005, Characterization of borehole fractures by the body and interface waves: Doctoral thesis, TU Delft, Delft University of Technology.

Henry, F., J. Fokkema, and C. de Pater, 2002, Experiments on Stoneley wave propagation in a borehole intersected by a finite horizontal fracture: 64th Annual International Conference and Exhibition, EAGE, Extended Abstracts, P143.

Holzhausen, G., and H. Egan, 1986, Fracture diagnostics in east Texas and western Colorado using the hydraulic-impedance method: Presented at the SPE Unconventional Gas Technology Symposium.

Holzhausen, G., and R. Gooch, 1985a, Impedance of hydraulic fractures: Its measurement and use for estimating fracture closure pressure and dimensions: Presented at the SPE/DOE Low Permeability Gas Reservoirs Symposium.

Holzhausen, G. R., and R. P. Gooch, 1985b, The effect of hydraulic-fracture growth on free oscillations of wellbore pressure: Presented at the 26th US Symposium on Rock Mechanics (USRMS), American Rock Mechanics Association.

Hornby, B., D. Johnson, K. Winkler, and R. Plumb, 1989, Fracture evaluation using reflected Stoneley-wave arrivals: Geophysics, **54**, 1274–1288, doi: 10.1190/1.1442587.

Ionov, A. M., 2007, Stoneley wave generation by an incident P-wave propagating in the surrounding formation across a horizontal fluid-filled fracture: Geophysical Prospecting, **55**, 71–82, doi: 10.1111/j.1365-2478.2006.00577.x.

Ionov, A. M., and G. A. Maximov, 1996, Propagation of tube waves generated by an external source in layered permeable rocks: Geophysical Journal International, **124**, 888–906, doi: 10.1111/j.1365-246X.1996.tb05643.x.

Karlstrom, L., and E. M. Dunham, 2016, Excitation and resonance of acoustic-gravity waves in a column of stratified, bubbly magma: Journal of Fluid Mechanics, **797**, 431–470, doi: 10.1017/jfm.2016.257.

Korneev, V., 2008, Slow waves in fractures filled with viscous fluid: Geophysics, **73**, no. 1, N1–N7, doi: 10.1190/1.2802174.

Korneev, V., 2010, Low-frequency fluid waves in fractures and pipes: Geophysics, **75**, no. 6, N97–N107, doi: 10.1190/1.3484155.

Kostek, S., D. L. Johnson, and C. J. Randall, 1998a, The interaction of tube waves with borehole fractures. Part I: Numerical models: Geophysics, **63**, 800–808, doi: 10.1190/1.1444391.

Kostek, S., D. L. Johnson, K. W. Winkler, and B. E. Hornby, 1998b, The interaction of tube waves with borehole fractures. Part II: Analytical models: Geophysics, **63**, 809–815, doi: 10.1190/1.1444392.

Krauklis, P. V., 1962, On some low-frequency oscillations of a fluid layer in an elastic medium: Journal of Applied Mathematics and Mechanics, **26**, 1685–1692, doi: 10.1016/0021-8928(62)90203-4.

Krauklis, P. V., and L. Krauklis, 1998, Excitation of a tube wave in a borehole by a slow wave propagating in a fluid layer: Journal of Mathematical Sciences, **91**, 2776–2781, doi: 10.1007/BF02433993.

Lawn, B., 1993, Fracture of brittle solids: Cambridge University Press.

Liang, C., E. Dunham, O. O'Reilly, and L. Karlstrom, 2015, A linearized model for wave propagation through coupled volcanic conduit-crack systems filled with multiphase magma: Presented at the 2015 AGU Fall Meeting.

Lipovsky, B. P., and E. M. Dunham, 2015, Vibrational modes of hydraulic fractures: Inference of fracture geometry from resonant frequencies and attenuation: Journal of Geophysical Research: Solid Earth, **120**, 1080–1107.

Livescu, S., S. Craig, and B. Aitken, 2016, Fluid-hammer effects on coiled-tubing friction in extended-reach wells: SPE Journal, SPE-179100-PA, doi: 10.2118/179100-PA.

MacPhail, W. F., B. Lisoway, and K. Banks, 2012, Fiber optic distributed acoustic sensing of multiple fractures in a horizontal well: Presented at the SPE Hydraulic Fracturing Technology Conference.

Mathieu, F., and M. Toksoz, 1984, Application of full waveform acoustic logging data to the estimation of reservoir permeability: Technical report, Massachusetts Institute of Technology, Earth Resources Laboratory.

Medlin, W., and D. Schmitt, 1994, Fracture diagnostics with tube wave reflection logs: Journal of Petroleum Technology, **46**, 239–248, doi: 10.2118/22872-PA.

Molenaar, M. M., D. Hill, P. Webster, E. Fidan, and B. Birch, 2012, First downhole application of distributed acoustic sensing for hydraulic-fracturing monitoring and diagnostics: SPE Drilling & Completion, **27**, 32–38, doi: 10.2118/140561-PA.

Mondal, S., 2010, Pressure transients in wellbores: Water hammer effects and implications for fracture diagnostics: Master's thesis, The University of Texas at Austin.

Nakagawa, S., 2013, Low-frequency (<100 Hz) dynamic fracture compliance measurement in the laboratory: Presented at the 47th US Rock Mechanics/Geomechanics Symposium, American Rock Mechanics Association.

Nakagawa, S., S. Nakashima, and V. A. Korneev, 2016, Laboratory measurements of guided-wave propagation within a fluid-saturated fracture: Geophysical Prospecting, **64**, 143–156, doi: 10.1111/1365-2478.12223.

Nikitin, A. A., B. D. Plyushchenkov, and A. Y. Segal, 2016, Properties of low-frequency trapped mode in viscous-fluid waveguides: Geophysical Prospecting, **64**, 1335–1349, doi: 10.1111/1365-2478.12306.

O'Reilly, O., E. Dunham, and D. Moos, 2014, Inferring the properties of fluid-filled fractures using tube waves: AGU Fall Meeting Abstracts, 4799.

Paige, R., L. Murray, and J. Roberts, 1995, Field application of hydraulic impedance testing for fracture measurement: SPE Production & Facilities, **10**, 7–12, doi: 10.2118/26525-PA.

Paige, R., J. Roberts, L. Murray, and D. Mellor, 1992, Fracture measurement using hydraulic impedance testing: Presented at the SPE Annual Technical Conference and Exhibition.

Paillet, F. L., 1980, Acoustic propagation in the vicinity of fractures which intersect a fluid-filled borehole: Presented at the SPWLA 21st Annual Logging Symposium, SPWLA-1980–DD.

Paillet, F., and J. White, 1982, Acoustic modes of propagation in the borehole and their relationship to rock properties: Geophysics, **47**, 1215–1228, doi: 10.1190/1.1441384.

Pardo, D., P. J. Matuszyk, C. Torres-Verdin, A. Mora, I. Muga, and V. M. Calo, 2013, Influence of borehole-eccentred tools on wireline and logging-while-drilling sonic logging measurements: Geophysical Prospecting, **61**, 268–283, doi: 10.1111/1365-2478.12022.

Patzek, T. W., and A. De, 2000, Lossy transmission line model of hydrofractured well dynamics: Journal of Petroleum Science and Engineering, **25**, 59–77, doi: 10.1016/S0920-4105(99)00055-8.

Power, W. L., and T. E. Tullis, 1991, Euclidean and fractal models for the description of rock surface roughness: Journal of Geophysical Research: Solid Earth, **96**, 415–424, doi: 10.1029/90JB02107.

Schoenberg, M., 1986, Fluid and solid motion in the neighborhood of a fluid-filled borehole due to the passage of a low-frequency elastic plane wave: Geophysics, **51**, 1191–1205, doi: 10.1190/1.1442174.

Shih, P.-J. R., and M. Frehner, 2015, Laboratory evidence for Krauklis wave resonance in a fracture and implications for seismic coda wave analysis: 85th Annual International Meeting, SEG, Expanded Abstracts, 3209–3213.

Tang, X., 1990, Acoustic logging in fractured and porous formations: Ph.D. thesis, Massachusetts Institute of Technology.

Tang, X. M., and C. H. Cheng, 1988, Wave propagation in a fluid-filled fracture an experimental study: Geophysical Research Letters, **15**, 1463–1466, doi: 10.1029/GL015i013p01463.

Tang, X. M., and C. H. Cheng, 1989, A dynamic model for fluid flow in open borehole fractures: Journal of Geophysical Research: Solid Earth, **94**, 7567–7576, doi: 10.1029/JB094iB06p07567.

Tary, J. B., M. van der Baan, and D. W. Eaton, 2014, Interpretation of resonance frequencies recorded during hydraulic fracturing treatments: Journal of Geophysical Research: Solid Earth, **119**, 1295–1315.

Tezuka, K., C. H. Cheng, and X. M. Tang, 1997, Modeling of low-frequency Stoneley-wave propagation in an irregular borehole: Geophysics, **62**, 1047–1058, doi: 10.1190/1.1444206.

Wang, X., K. Hovem, D. Moos, and Y. Quan, 2008, Water hammer effects on water injection well performance and longevity: Presented at the SPE International Symposium and Exhibition on Formation Damage Control, SPE 112282–PP.

Yamamoto, M., and H. Kawakatsu, 2008, An efficient method to compute the dynamic response of a fluid-filled crack: Geophysical Journal International, **174**, 1174–1186, doi: 10.1111/j.1365-246X.2008.03871.x.

Ziatdinov, S., B. Kashtan, and A. Bakulin, 2006, Tube waves from a horizontal fluid-filled fracture of a finite radius: 76th Annual International Meeting, SEG, Expanded Abstracts, 369–373.